Weierstraß-Institut
für Angewandte Analysis und Stochastik

im Forschungsverbund Berlin e.V.

Preprint ISSN 0946 – 8633

Unsteady Thermal Convection in the North-East German Basin

Ulf Bayer, Volker Clausnitzer, and Jürgen Fuhrmann

submitted: May 27, 2002

No. 741
Berlin 2002

1991 *Mathematics Subject Classification.* 65N99, 76R10.
Key words and phrases. Thermal Convection, Finite Volumes, Nonlinear Time Series Analysis.

Edited by
Weierstraß-Institut für Angewandte Analysis und Stochastik (WIAS)
Mohrenstraße 39
D — 10117 Berlin
Germany

Fax: + 49 30 2044975
E-Mail: preprint@wias-berlin.de
World Wide Web: http://www.wias-berlin.de/

ABSTRACT. We describe a Voronoi box based finite volume method for the numerical simulation of thermal convection in sedimental basins. The method shows a temperature maximum principle and consistent velocity approximation. We present results of simulation runs in vertical slices of the North-East German basin. These indicate that the system is far from a stationary state, it shows quasi-periodic, and possibly chaotic behaviour. The chaos hypothesis is formulated based on the analysis of the Nusselt number time series obtaind from simulation runs.

1. INTRODUCTION

Extensive evidence for rising saline waters is available on a regional scale within the North German Basin with more than 100 reported locations of saline springs. A common characteristic of these springs is their temporal and spatial instability (vagabonding springs) - approximately one tenth of the springs are known only from historical notes and presently cannot be observed.

For Schleswig-Holstein, Heck [Hec32] lists various locations of saltwater presence at the surface, which cannot be explained as originating from any shallow salt deposits or salt domes and whose cause therefore remains unknown. A lack of explanation is also noted by Johannsen [Joh80] for steep vertical plumes of saline fluids observed in Schleswig-Holstein that reach near-surface levels. In addition, there is no indication of related faults or high-permeability conduits. Even assuming that such preferential pathways do exist, the physical driving force for the upward flow of saline fluids still remains to be identified.

Hannemann and Schirrmeister [HS98] compared the chemistry of deep groundwater levels with the chemistry of the vagabonding springs and concluded that they originated mainly in the deeper, Pre-Tertiary sub-ground. They then hypothesize, that high-permeability pathways exist and that Quartenary long-term fluctuations of the sea level are responsible for vertical exchange of saline and fresh water due to the changing hydraulic pressure gradients within the basin. However, the low topography of Brandenburg and Schleswig-Holstein does not account for a differentiated hydraulic head which could support the vagabonding springs. The concept of [HS98] therefore, should produce more evenly distributed replacements on a regional level. The steep rising plumes described in [Joh80] in particular point to the possibility of significant temperature effects on the fluid density and possible free convection. Numerical calculations [SSH99] in a rectangular cavity with material parameters from the deep geosphere support this hypothesis.

The aim of this paper is to present first results of numerical experiments with data from the North-East-German Basin which indeed hint into this direction. We present a thermoconvective flow model based on a finite volume method which is able to handle heterogeneous, layered geometries, showing consistent velocity approximation and temperature maximum principle, we address meshing issues and we present results of transient two-dimensional numerical calculations. We evaluate the solutions based on the Nusselt number time series. Using spectral analysis and time series analysis tools, we try to discriminate between stationary, quasi-periodic and chaotic flow regimes. We discuss open issues in connection with this approach.

2. Model Equations

The model considered consists of the Darcy law without inertia terms, which together with a mass balance equation describes the movement of a fluid in a saturated porous medium, and the Fourier law with convection which together with an energy balance models the movement of heat energy in a mixture of fluid and solid phase. In [NB98] one finds an exhausting discussion of this type of models. In a d-dimensional domain Ω consider

$$\text{mass balance:} \quad \partial_t(\varphi\tilde{\rho}_f) - \nabla\cdot(\tilde{\rho}_f\mathbf{v}) = 0 \tag{2.1a}$$

$$\text{Darcy law:} \quad \mathbf{v} = \frac{k}{\mu}(\nabla p - \rho_f\mathbf{g}) \tag{2.1b}$$

$$\text{energy balance:} \quad \partial_t(((1-\varphi)\rho_s c_s + \varphi\tilde{\rho}_f c_f)T) - \nabla\cdot\mathbf{q} = 0 \tag{2.1c}$$

$$\text{Fourier law:} \quad \mathbf{q} = (\varphi\lambda_f + (1-\varphi)\lambda_s)\nabla T - T\tilde{\rho}_f c_f\mathbf{v} \tag{2.1d}$$

The basic unknowns are the pressure p and the temperature T of the fluid. All other symbols are explained in appendix A. The data of the fluid – density ρ and viscosity μ – can depend on pressure and temperature. All data of the porous matrix can have spatial variations. Througout the paper, we assume that our computational domain is subdivided into layers of different materials, and that we can assume constant matrix data for each of the layers.

We assume that the boundary $\partial\Omega$ is subdivided into non-intersecting parts Γ_i wich are due to different boundary conditions, namely either

$$\text{impermeable:} \quad \mathbf{v}\cdot\mathbf{n} = 0 \quad \text{or} \tag{2.2a}$$

$$\text{free:} \quad p = p_{\Gamma_i}(\mathbf{x}) \tag{2.2b}$$

for (2.1a)-(2.1b), and either

$$\text{insulating:} \quad \mathbf{q}\cdot\mathbf{n} = 0 \quad \text{or} \tag{2.3a}$$

$$\text{conducting:} \quad T = T_{\Gamma_i}(\mathbf{x}) \tag{2.3b}$$

for (2.1c)-(2.1d). For a more detailed discussion of boundary conditions and geometries see section 4.

For the density of water, use assume that $\tilde{\rho} = \rho = \rho(p,T), \mu = \mu(T)$ according to appendix C, unless we regard for theoretical and verification reasons the Boussinesq approximation.

The Boussinesq approximation assumes that $\tilde{\rho}_f = \rho_{\text{ref}}$ is constant, and the fluid is incompressible, hence the only temperature dependent term in the pressure equation remains the factor at the gravity term in the Darcy law (2.1b). It is believed that in this case, the main physical effects still are in the model. In the two-dimensional case, this approximation often is the base for a stream function formulation of the problem [NB98], also exploited in numerical methods, see e.g. [HY95].

The Boussinesq case allows for a dimensionless formulation [NB98] which in the case of a homogeneous rectangular domain reduces the set of model parameters to two dimensionless values, namely the Rayleigh number (4.3) and the aspect ratio. Quite a lot is known in this case about the transition from steady state to convection. Moreover, in this case it was possible to give an existence proof for the continuous solution, and to estimate the dependency of the dimension of the attractor of the system in dependence on the Rayleigh number [EFZ00].

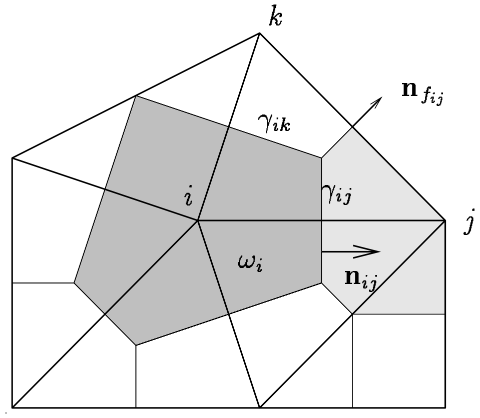

FIGURE 2.1. Geometrical coefficients of the finite volume scheme

Here, we include this model for the purpose of verification of the code and because in this case we are able to prove some qualitaive results about the discretization we use.

3. NUMERICAL METHOD

3.1. **Finite volume discretization: general ansatz.** Here, we describe our finite volume discretization ansatz for heterogeneous domains. For the convenience of the reader, we describe the method for the two- dimensional case, but in fact, all formulations can be extended to one and three space dimensions by dimension-independent notations. Our description here stays mainly on the verbal level, for a mathematically more rigorous introduction in the scalar case see [FL01]. Apparantly, the oldest reference to the method is found in [Mac53].

Assume that the computational domain is the union of a finite number of subdomains which correspond to the different geological layers:

$$\Omega = \bigcup \sum_{m \in \mathcal{M}} \Omega_m$$

Let there be given a Delaunay triangulation conforming to the exterior and interior boundaries [BE95]. In the two-dimensional case, this means:

- The whole domain is the union of non-intersecting each other triangles.
- If a point is the node of a triangle, it is a node of all neigbouring triangles.
- Each triangle belongs to exactly one subdomain Ω_m.
- If two triangles share an edge, the sum of the angles opposite to that edge is less or equal than π.
- If a triangle shares an edge with an interior or exterior boundary, the angle opposite to that edge is less or equal than $\frac{\pi}{2}$.

Then we can set up the Voronoi boxes ω_i by joining the circumcenters of the simplices as in fig. 2.1. The box interfaces are denoted by γ_{ij}. Their (possibly empty) intersections with the domains Ω_m result in the items ω_i^m and γ_{ij}^m, respectively.

We will describe the finite volume scheme for the following class of problems: We look for a vector valued function $u(x,t) : \Omega \times [0,T] \to \mathbb{R}^\nu$ such that

$$
\begin{aligned}
&\partial_t b(u) + \nabla \cdot \mathbf{j}(u) = 0 \\
&\qquad\qquad \mathbf{j}(u) = -k(u)\nabla u + \mathbf{w}(u).
\end{aligned}
\tag{3.1}
$$

Here, $b(\cdot), k(\cdot) : \mathbb{R}^\nu \to \mathbb{R}^\nu$ are vector valued functions depending on vectors, and $\mathbf{j}(\cdot), \mathbf{w}(\cdot) : \mathbb{R}^\nu \to \mathbb{R}^{\nu d}$ are $\nu \times \nu$-tensor valued functions.

Introducing the vector valued flux functions

$$g^m(\mathbf{h}, u, v) = (g_1^m(\mathbf{h}; u_1 \dots u_\nu; v_1 \dots v_\nu) \dots g_\nu^m(\mathbf{h}; u_1 \dots u_\nu; v_1 \dots v_\nu))$$

which should be approximations to the cell-to-cell fluxes generated by the projection of the main part of our system onto the mesh edges, we can approximate the balance of the l-th equation of (3.1) over the space-time cell $\omega_i \times (t_n, t_{n+1})$ by:

$$
\begin{aligned}
0 &= \int_{t^n}^{t^{n+1}} \int_{\omega_i} \left(\frac{\partial b_l(x,u)}{\partial t} + \nabla \cdot \mathbf{j}_l \right) d\omega d\tau \\
&\approx \sum_{m \in \mathcal{M}} |\omega_i^m| \left(b_l^m(u_i^{n+1}) - b_l^m(u_i^n) \right) + \\
&\quad + \tau^n \sum_{m \in \mathcal{M}} \sum_{j \in \mathrm{nb}_{\mathcal{N}}(i)} \frac{|\gamma_{ij}^m|}{h_{ij}} g^m_{\mathbf{h}_{ij};l}(u_i^{n+1}, u_j^{n+1})
\end{aligned}
\tag{3.2}
$$

The main idea is to cast the volume integral of the flux divergence into a surface integral of the normal flux, to split this up into the material parts and to replace the normal flux by the flux function. The problem now is characterized by the mass terms b and flux function g corresponding to each material. The approximation chosen corresponds to an implicit Euler scheme. An existence and stability analysis of this scheme for the scalar case has been carried out in [FL01].

3.2. **Finite volume discretization of thermal convection.** To approximate system (2.1a)-(2.1d) we first show that it fits into the problem class (3.1). Indeed, let $u = (p,T)$, and denote

$$
\begin{aligned}
b_1^m(p,T) &= \varphi^m \tilde{\rho}_f(p,T) \\
b_2^m(p,T) &= ((1-\varphi^m)\rho_s^m c_s^m + \varphi^m \tilde{\rho}_f c_f)T \\
\mathbf{j}_1(p,T) &= \frac{k^m \tilde{\rho}_f}{\mu}(\nabla p - \rho_f \mathbf{g}) \\
\mathbf{j}_2(p,T) &= (\varphi^m \lambda_f + (1-\varphi^m)\lambda_s^m)\nabla T - T c_f \mathbf{j}_1(p,T).
\end{aligned}
\tag{3.3}
$$

Let $\rho_i = \rho_f(p_i, T_i)$,$\tilde{\rho}_i = \tilde{\rho}_f(p_i,T_i)$, $\mu_i = \mu(T_i)$, $\lambda^m = (\varphi^m \lambda_f + (1-\varphi^m)\lambda_s^m)$. Further, let $B(\xi) = \frac{\xi}{e^\xi - 1}$ be the Bernoulli function.

In order to discretize (2.1b), we choose the following ansatz:

$$g_1^m = g_1^m(\mathbf{h}, (p_1,T_1), (p_2,T_2)) = k^m \frac{\tilde{\rho}_1 + \tilde{\rho}_2}{\mu_1 + \mu_2} \left(p_1 - p_2 - \frac{\rho_1 + \rho_2}{2} \mathbf{g} \cdot \mathbf{h} \right)$$

Exponential fitting [AS55, Il'69, SG69] is used for (2.1d) and leads to

$$g_2^m = g_2^m(\mathbf{h}, (p_1,T_1), (p_2,T_2)) = \lambda^m \left(B(\frac{\rho_f c_f g_1^m}{\lambda^m})T_1 - B(-\frac{\rho_f c_f g_1^m}{\lambda^m})T_2 \right)$$

The functions $b_1^m, b_2^m, g_1^m, g_2^m$ together with (3.2) completely describe the discretization ansatz used.

3.3. **Properties of the discretization.**

3.4. **Theorem.** *(Consistent velocity approximation.) For an incompressible fluid with density linearily depending on temperature in a homogeneous aquifer, the nodal projection of the diffusive steady state solution of the continuous system is a solution of the discrete problem .*

Proof. Let $\rho_f = \rho_{\mathrm{ref}} + \beta_T(T - T_{\mathrm{ref}})$ and $\lambda = \varphi\lambda_f + (1-\varphi)\lambda_s)$. The solution mentionend then is described by the system

$$\mathbf{v} = \frac{k}{\mu}(\nabla p - \rho_f \mathbf{g}) = 0 \tag{3.5a}$$

$$-\nabla \cdot \lambda \nabla T = 0 \tag{3.5b}$$

Let $\mathbf{g} = g\mathbf{n}_g$ and assume that ξ is defined by $\mathbf{x} = \mathbf{x}(\xi) = \mathbf{x}_0 + \xi\mathbf{n}_g$. Let $\bar{p}(\xi) = p(\mathbf{x}(\xi))$ and $\bar{T}(\xi) = T(\mathbf{x}(\xi))$. Substituting this ansatz yields

$$\bar{p}' - g\rho_f(\bar{T}) = 0 \tag{3.6a}$$

$$-\lambda\bar{T}'' = 0 \tag{3.6b}$$

The general solution of the temperature equation then has the form $T = T_0 + C\xi$ with T_0, C being constants. For $\rho_0 = \rho_{\mathrm{ref}} + \beta_T(T - T_0)$ we get

$$\rho_f = \rho_0 + \beta_T(\bar{T} - T_0) = \rho_0 + \beta_T C\xi.$$

yielding the pressure eaquation

$$\bar{p}' - g\rho_0 - g\beta_T C\xi = 0$$

with the general solution

$$\bar{p}(\xi) = p_0 + g\rho_0\xi + \frac{1}{2}g\beta_T C\xi^2$$

For two neigboring discretization nodes $\mathbf{x}_i, \mathbf{x}_j$, let $\xi_i = \mathbf{x}_i \cdot \mathbf{n}_g$. In this case, for $\mathbf{h} = \mathbf{x}_i - \mathbf{x}_j$, $\mathbf{g} \cdot \mathbf{h} = \xi_i - \xi_j$. consequently,

$$\begin{aligned}
g_1 &= k\frac{\rho_i + \rho_j}{\mu_i + \mu_j}(p_i - p_j - \frac{\rho_i + \rho_j}{2}(\xi_i - \xi_j)) \\
&= k\frac{\rho_i + \rho_j}{\mu_i + \mu_j}(g\rho_0(\xi_i - \xi_j) + \frac{1}{2}g\beta_T C(\xi_i^2 - \xi_j^2) \\
&\qquad - g\rho_0(\xi_i - \xi_j) - \frac{1}{2}g\beta_T C(\xi_i + \xi_j)(\xi_i - \xi_j)) \\
&= 0
\end{aligned}$$

Further, due to $B(0) = 1$, we have

$$g_2 = \lambda(\xi_i - \xi_j) = \lambda\mathbf{h}_{ij} \cdot \mathbf{n}_g$$

Putting this into the ith nodal equation yields

$$\sum_{j \in \mathrm{nb}_{\mathcal{N}}(i)} \frac{|\gamma_{ij}|}{h_{ij}}\mathbf{h}_{ij} \cdot \mathbf{n}_g = \sum_{j \in \mathrm{nb}_{\mathcal{N}}(i)} |\gamma_{ij}|\mathbf{n}_{ij} \cdot \mathbf{n}_g = \int_{\partial\omega_i} \mathbf{n}_g \cdot \mathbf{n}\, ds = \int_{\omega_i} \nabla \cdot \mathbf{n}_g\, d\omega = 0$$

Consequently, we obtained a solution of the discrete system. □

This result includes the case of Boussinesq approximation. We remark that this problem has been addressed in [Fro98a] for a finite volume method with differently defined control volumina where the issue had been resolved by using finite element interpolations of different degrees.

One could choose an upwind evaluation of the density in the gravitation term in oder to get a maximum principle for the pressure in the incompressible case. In this case, we would lose the consistent velocity approximation. On coarse unstructured meshes we then would be unable to decide about the onset of convection. Instead, as the discrete stationary solution is not convection free, we would see grid effects interplaying with the onset of convection.

3.7**. Theorem.** *(Maximum principle.) For the discretized Boussinesq approximation, in each non-Dirichlet node, a temperature maximum principle is valid:*

$$T_i^n \leq \max\{T_i^{n-1}\} \bigcup_{j\in \mathrm{nb}(i)} \{T_j^n\}$$

$$T_i^n \geq \min\{T_i^{n-1}\} \bigcup_{j\in \mathrm{nb}(i)} \{T_j^n\}$$

Proof. For the proof, we use the methodology of [FL01]. First, we state the pressure equation for the Boussinesq case:

$$\sum_{j\in \mathrm{nb}_{\mathcal{N}}(i)} \frac{|\gamma_{ij}|}{h_{ij}} g_1((p_i,T_i),(p_j,T_j)) = 0. \tag{3.8}$$

Define

$$g_2^*(\Theta_i,\Theta_j) = \lambda^m \left(B(\frac{\rho_f c_f g_1^m((p_i,T_i),(p_j,T_j))}{\lambda^m})\Theta_1 - B(-\frac{\rho_f c_f g_1^m((p_i,T_i),(p_j,T_j))}{\lambda^m})\Theta_2 \right)$$

We note, that

$$k_{ij} = \frac{|\gamma_{ij}|}{h_{ij}} \frac{g_2^*(\Theta_i,\Theta_j) - g_2^*(\Theta_i,\Theta_i)}{\Theta_i - \Theta_j} \geq 0, \tag{3.9}$$

because of the nonnegativity of the Bernoulli function (we can extend the definition by continuity to $\Theta_i = \Theta_j$) and

$$g_2^*(\Theta_i,\Theta_i) = \tilde{\rho_f} c_f g_1((p_i,T_i),(p_j,T_j)) \tag{3.10}$$

because of the addition theorem $B(\xi) + B(-\xi) = 1$. Further, we have

$$g_2^*(T_i,T_j) = g_2(T_i,T_j)$$

The temperature equation writes as

$$\begin{aligned} c|\omega_i|(T_i^n - T_i^{n-1}) &= \sum_{j\in \mathrm{nb}_{\mathcal{N}}(i)} \frac{|\gamma_{ij}|}{h_{ij}} (g_2^*(T_i,T_j) - g_2^*(T_i,T_i)) + \sum_{j\in \mathrm{nb}_{\mathcal{N}}(i)} \frac{|\gamma_{ij}|}{h_{ij}} g_2^*(T_i,T_i) \\ &= \sum_{j\in \mathrm{nb}_{\mathcal{N}}(i)} \frac{|\gamma_{ij}|}{h_{ij}} \frac{g_2^*(T_i,T_j) - g_2^*(T_i,T_i)}{T_i - T_j} (T_i - T_j) \\ &\quad + \sum_{j\in \mathrm{nb}_{\mathcal{N}}(i)} \frac{|\gamma_{ij}|}{h_{ij}} \tilde{\rho}_f c_f g_1((p_i,T_i),(p_j,T_j)) \\ &= \sum_{j\in \mathrm{nb}_{\mathcal{N}}(i)} k_{ij}(T_i^n - T_j^n) \end{aligned}$$

Consequently, we have

$$T_i^n = \frac{c|\omega_i| T_i^{n-1} + \sum\limits_{j \in \mathrm{nb}_{\mathcal{N}}(i)} k_{ij} T_j^n}{c|\omega_i| + \sum\limits_{j \in \mathrm{nb}_{\mathcal{N}}(i)} k_{ij}}$$

As all coefficients on the right hand side are nonnegative and less than 1 we get the desired result. □

Consequently, the temperature is allowed to take local extremal values only in nodes which had been intitialised this way, or at the boundary. Please note that this result is strongly related with the Delaunay property of the mesh which ensures that the expressions evaluated in order to yield the transfer coefficient $|\gamma_{ij}|$ stay nonnegative. For a treatment of this issue in connection with density driven flow with different types of control volumina, see [Fro98b].

In the non-Boussinesq case, the maximum principle is lost. However, as we still can assume that local density variations are small, large scale deviations from the maximum principle should not occur.

3.4. **Meshing.** The geometries we deal with are described by piecewise linear straight line graphs (PLSG) after processing measured data at GFZ [Sch97b, Sch97a, SB99]. The Delaunay refinement algorithm of Rupert and Shewchuk [Rup95, She97] in a constructive manner garantees the existence of a triangulation of such geometries obeying the properties described in subsection 3.1. Moreover, with the *triangle* code [She96], a tool is available which implements this algorithm in an efficient manner. It has been used to generate the meshes for the presented calculation. Besides of the boundary and layer interface information obtained from the geological data, the main parameter to influence the mesh has been the maximal area of a triangle.

In section 4, we perform calculations on two slices of the basin geometry, one of of length 35 km, the other of length 105 km, both of depth approximately 6 km. There approximate placement in the region of the North-East German basin can be seen in fig 3.1. The meshes are depicted in figure 3.2. We controlled the *triangle* mesh generator by calculating a maximum area from a given maximum edge length denoted by h throughout the paper.

3.5. **Time step control.** We use an adaptive time step control scheme which is aimed at holding the L^∞ norm of the change of the solution constant over all timesteps. There are two exceptions from the time step control scheme. First, this scheme appears to be to insensitive to catch the periodic behaviour described below, so we had to introduce a maximal timestep chosen quite tightly. Second, the timestep size is lowered if Newton's method fails for a given timestep.

3.6. **Equation Solver.** In each time step, we have to solve a system of nonlinear equations. This is done using Newton's method [KA59] using an affine invariant monotonicity test [DH79]. In the presented numerical examples, we use the direct sparse matrix solver PARDISO [SGF00], and we solved the nonlinear equations up to machine precision.

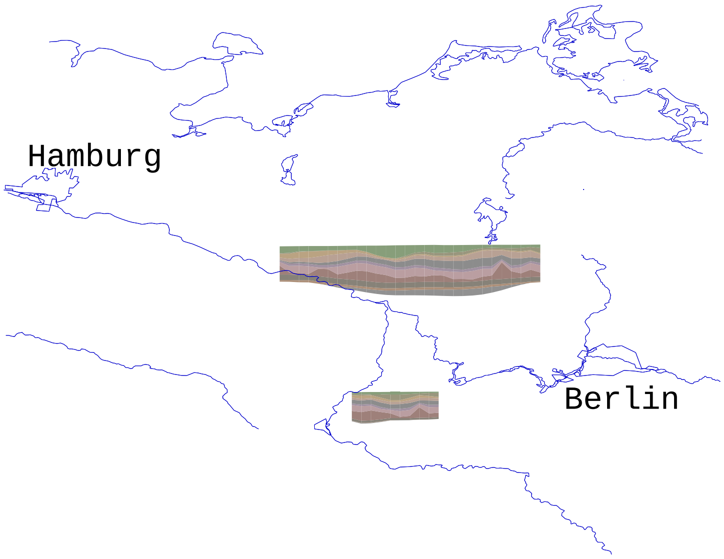

FIGURE 3.1. Map of North-East German basin

3.7. **Implementation.** The methods described have been implemented in the pdelib/sysconlaw code [FKL01, Fuh02] for the solution of nonlinear systems of viscous conservation laws.

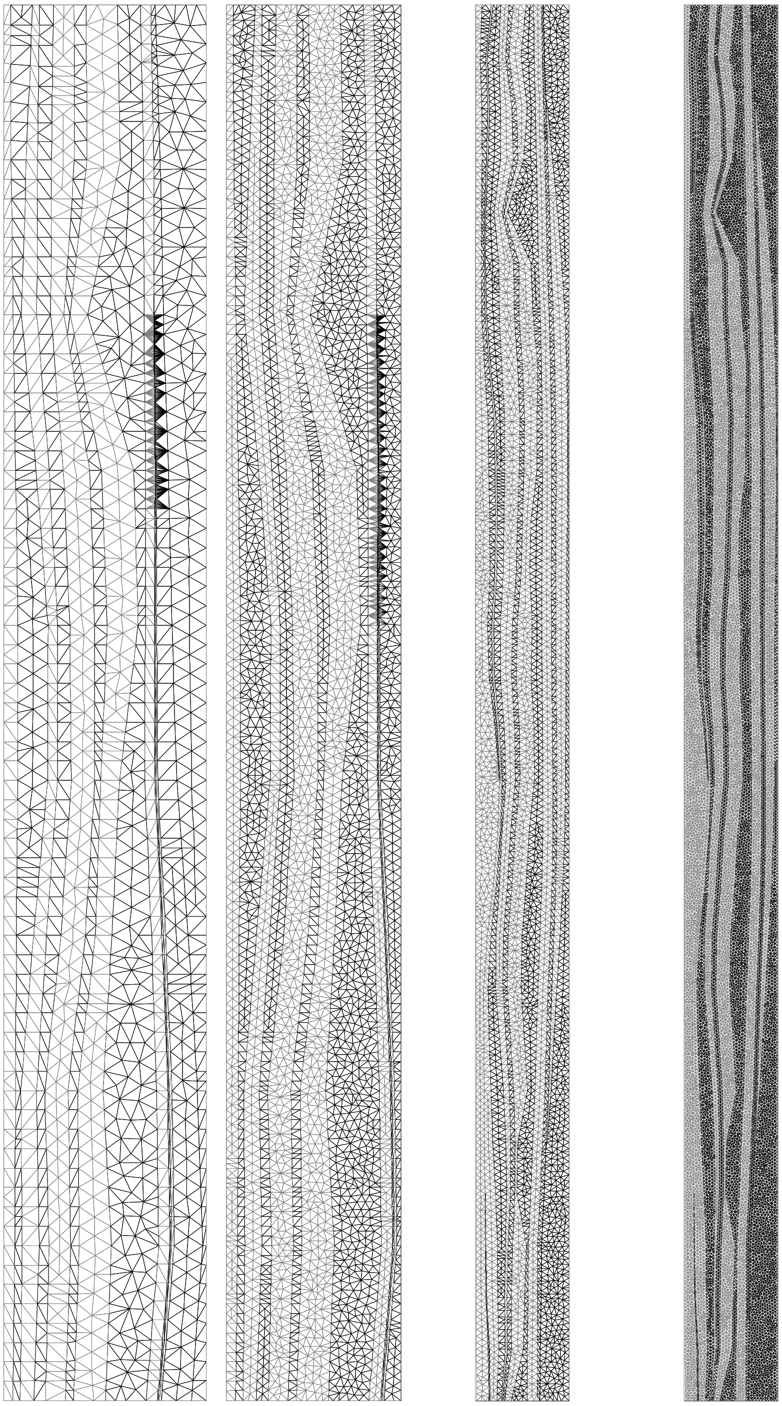

Slice 1, h=500m 1918 nodes

Slice 1, h=250m 4833 nodes

Slice 2, h=500m 5203 nodes

Slice 2, h=250m 18468 nodes

FIGURE 3.2. Meshes

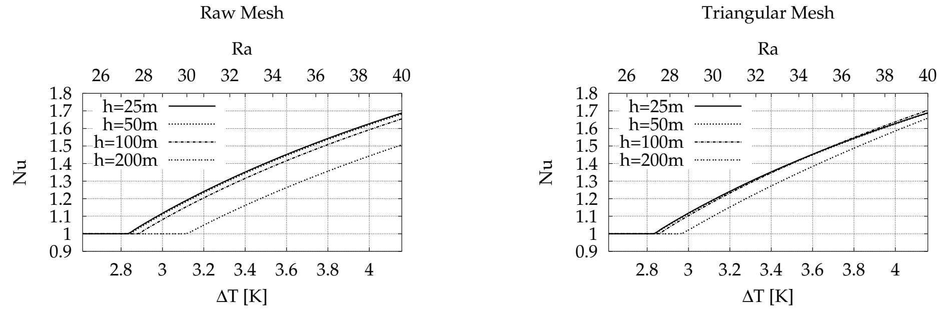

FIGURE 4.1. Onset of convection for rectangular cavity (Boussinesq approximation)

4. NUMERICAL RESULTS

All numerical results are obtained by a very straightforward randomized path following method. By this, we mean the following: Starting with some initial temperature gradient, we obtain a some solution (stationary or oscillating). Oscillatig solutions are calculated for 10Ma. After a solution has been obtained, we increase the temperature gradient by some amount by increasing the bottom heating temperature. As an initial state for the new transient calculation we take the last obtained solution with some random perturbation.

By this, we hope to leave solution branches as soon as they become unstable, in oder to attach stable branches which are more likely to be realized in nature.

As a main characteristic of the solution, we take the Nusselt number. It describes the ratio between overall heat transfer and diffusive heat transfer. For a solution with no convection, $Nu = 1$. Otherwise, $Nu > 1$.. In our case, we can define the Nusselt number as

$$Nu = \frac{\int_{\Gamma_{\text{top}}} \mathbf{q} \cdot \mathbf{n} ds}{\int_{\Gamma_{\text{top}}} \mathbf{q}_D \cdot \mathbf{n} ds} \tag{4.1}$$

where the diffusive heat flux $\mathbf{q}_D$ is defined as

$$\mathbf{q}_D = \lambda \nabla T = \mathbf{q} - T \tilde{\rho}_f c_f \mathbf{v} \tag{4.2}$$

and Γ_{top} denotes the upper boundary of the domain.

4.1. **Rectangular Cavity.** The first results we present in order to verify the code: we check for the consistent velocity approximation which takes place if the purely diffusive solution is realized independently of the mesh, and we verify that the first bifurcation takes place at the right parameter value.

We regard a rectangular cavity filled with porous material and saturated with water heated from below with a height of $H = 1000m$, an aspect ratio of 5 and porous medium data taken from the Kaenozoikum layer. It is triangulated in two ways: by a "raw" rectangular grid with given cell side length, and by a "truly unstructured triangular" grid generated using the *triangle* code with a given maximum area of triangles. We fix the temperatures at the top and the bottom boundaries and the pressure at the top. All other boundaries are assumed to be insulating and impermeable.

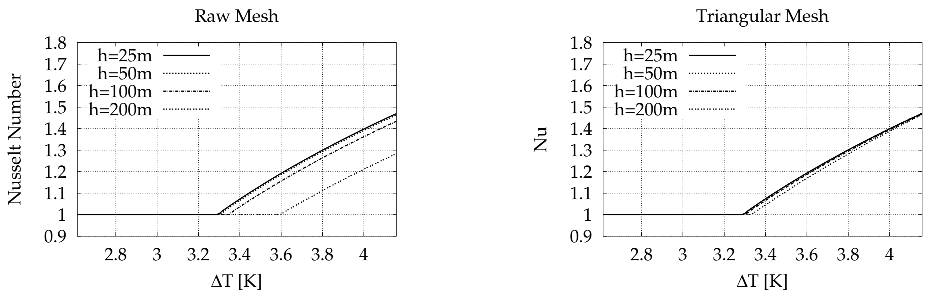

FIGURE 4.2. Onset of convection for rectangular cavity (Full model (C.2), (C.1))

According to [NB98], we can define the Rayleigh number Ra by

$$Ra = \Delta T \frac{\rho_f^2 c_f g k \beta_T H^2}{\mu(\phi\lambda_f + (1-\phi)\lambda_s)}. \tag{4.3}$$

4.1.1. *Onset of Convection.* In the case of an infinite horizontal layer, this problem is known as the Horton-Rogers-Lapwood problem [NB98]. It has been estimated that for the Boussinesq approximation, the bifurcation from the stable pure diffusive solution to a convective solution takes part at a Rayleigh number of 27.10, see [NB98]. This in our case would correspond to a temperature gradient of $2.85K/km$. As the geological temperature gradient is much higher, it is realistic to expect convective flow fields in many locations of the geometry.

In the simulations performed, this critical value is approximated better as grids become finer, both in the triangular mesh case and the raw mesh case, as shown in figure 4.1. This confirms that our numerical method performes correctly on this problem. Especially, in the triangular case, the consistency of the velocity approximation according to theorem 3.4 is verified.

In figure 4.2, we see that the first bifurcation point moves to higher temperatures – approximately $3.3K/km$ – if we use the full model with constitutive relationships (C.2), (C.1). We also notice (at least visually) grid convergence of the bifurcation point. In this case, a definition of the Rayleigh number is not anymore straightforward, thus from now on, we stop using this number, the more as later on, we will have to deal with complicated geometries.

4.1.2. *Onset of Oscillatory Convection.* To stay focused on the application, we provide only results for the full model.

In figure 4.3, we see the time average of the Nusselt number and the frequency corresponding to the maximum in the power spectrum obtained with the Lomb periodogram – a generalization of the power spectrum obtained by Fourier transformation for the case of non-equidistant meshes [Lom76, Moo00] – on two subsequent grids.

We clearly see a jump of the average Nusselt number in the region of a temperature gradient of $7.3 \ldots 7.5K/km$. Connected with this jump of the Nusselt number is the onset of oscillatory convection expressed by a nonzero basic frequency of oscillations. With increasing temperature, this basic frequency increases.

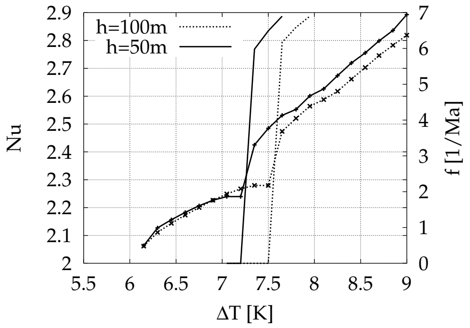

FIGURE 4.3. Onset of oscillatory convection

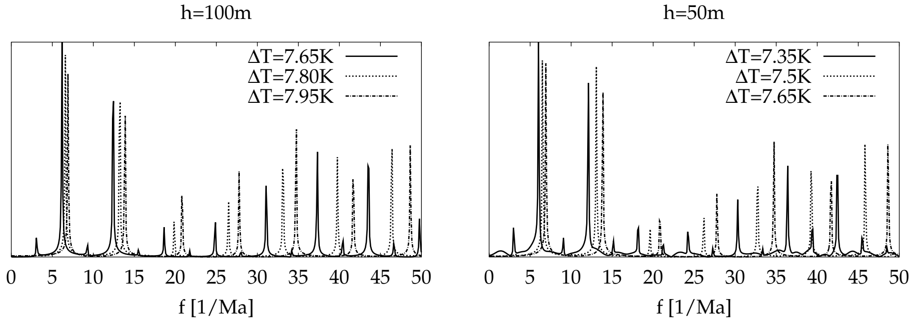

FIGURE 4.4. Lomb periodograms of oscillating solutions

FIGURE 4.5. Periodic and chaotic solutions after 10 Ma

Figure 4.4 shows the power spectra of the oscillating solutions for two subsequent meshes and different temperature values, showing visually the same qualitative behaviour.

4.1.3. *Onset of Chaos.* By chaos, we understand an aperiodic oscillatory behaviour of a deterministic system which at the same time sensitively depends on initial conditions. We can state chaotic behaviour of a given system just by visual evidence, however a more correct approach is to characterize the system state by so called invariant measures. Chaotic behaviour in a stronger mathematical sense then can be stated if these measures lie in a certain range. This way, we hopefully are able to distinguish the stated type of chaos from stochastical behaviour and from oscillations caused by bad numerical approximation. Establishing methods to obtain these measures efficiently in the case of data obtained from numerical solution of a PDE system is a task for forthcoming research activity.

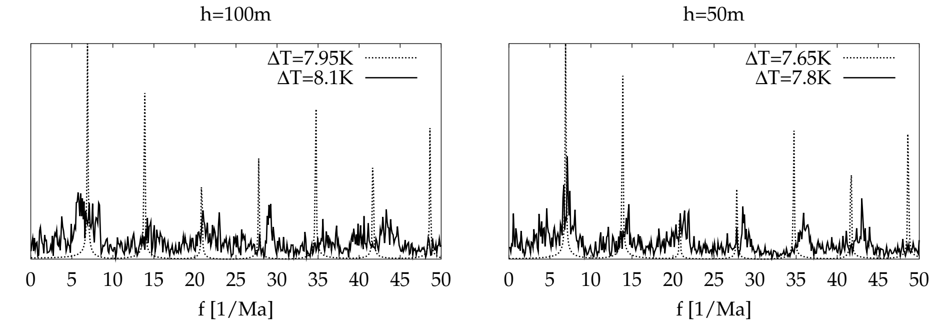

FIGURE 4.6. Lomb periodograms of periodic and chaotic solutions with close parameters

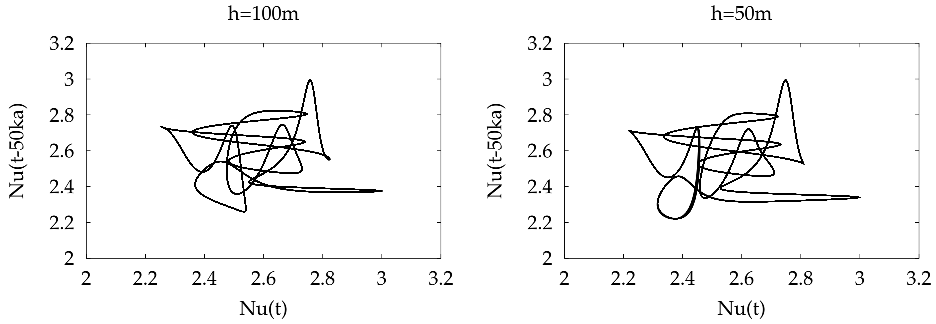

FIGURE 4.7. Phase portrait reconstruction of periodic solutions

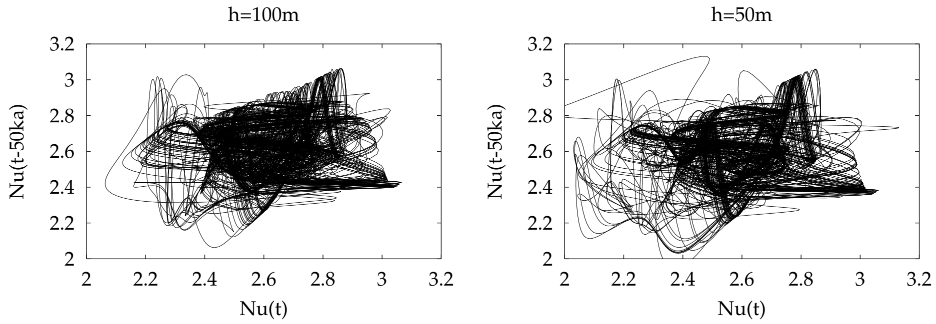

FIGURE 4.8. Phase portrait reconstruction of chaotic solutions

However, a first insight into these phenomena can be obtained by nonlinear time series analysis [KS97]. The basic tool is the time delay embedding which consists in obtaining an image of the system's phase space trajectory in an d-dimensional space by combining the values of the time series of a functional of the system's state with d time shifts of the same series. An illustration for $d = 2$ we se in 4.7.

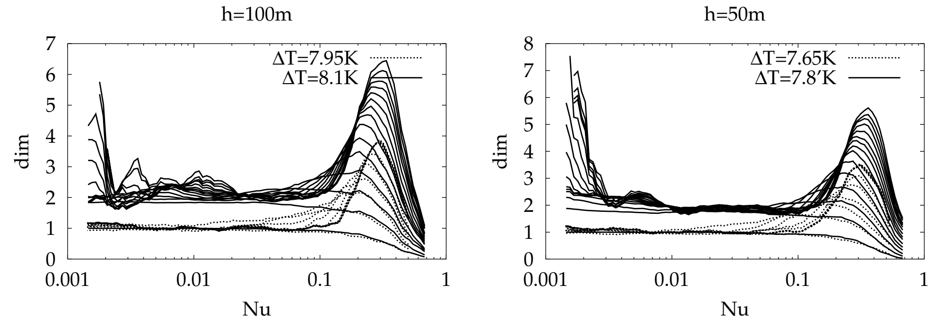

FIGURE 4.9. Estimate of correlation dimension of periodic and chaotic solutions with close parameters

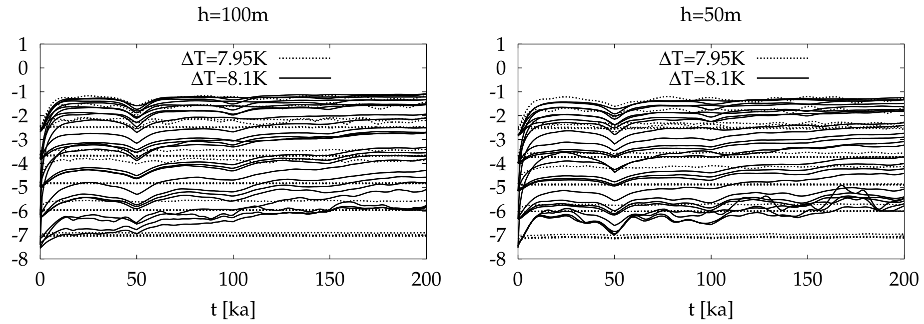

FIGURE 4.10. Estimate of maximal Lyapunov exponent of periodic and chaotic solutions with close parameters

Taken's famous embedding theorem [Tak81] states that under some generality assumptions, if d is large enough, the image obtained from the delay embedding is topologically equivalent to the origin in the phase space, thus bearing the same invariant measures. Consequently, it is sufficient to estimate invariant measures for the phase space reconstruction in oder to get an estimate of the invariant measures of the original system. We apply this methodology here on the base of the TISEAN software package [HKS99].

Figures 4.6 shows the power spectra of the last periodic and the first chaotic solution. On onset of chaos, we still see some dominating frequencies in the system indicating that there could be some kind of continuity in the transition. Figures 4.7 and 4.8 show the two-dimensional time delay embeddings of the time series. So far, chaos appears to be visually evident.

A more precise verification of chaotical behaviour can be given by estimates of the correlation dimension d_2 and the maximal Lyapunov exponent from the delay embedding of the Nusselt number time series.

Figure 4.9 shows the scaling range of the correlation dimension estimater `d2` from the TISEAN package. For the both the periodic and the chaotic solutions, we see a clear scaling range which indicates that the estimator works correctly. According to [HKS99] we can deduce a correlation dimension of 1 for the periodic solution, and an correlation dimension estimate of slightly below 2 for the chaotic solution.

Figure 4.10 shows the estimate of the maximal Lyapunov exponent by the `lyap_k` estimator from TISEAN. We can read the Lyapunov exponent from the slope of the estimator curves. The periodic solutions have a well estimated maximal Lyapunov exponent of 0, while the "chaotic" solutions show a positive maximal Lyapunov exponent, thus confirming the chaos hypothesis.

From the figures 4.9,4.10 we can conclude, that the visual evidence of chaos is supported by the observation that time series estimates of two important invariant measures of the system lie in the range which indicates chaotic behaviour. A further confirmation we obtain from the fact that these results are similar on two meshes with different spatial resolution.

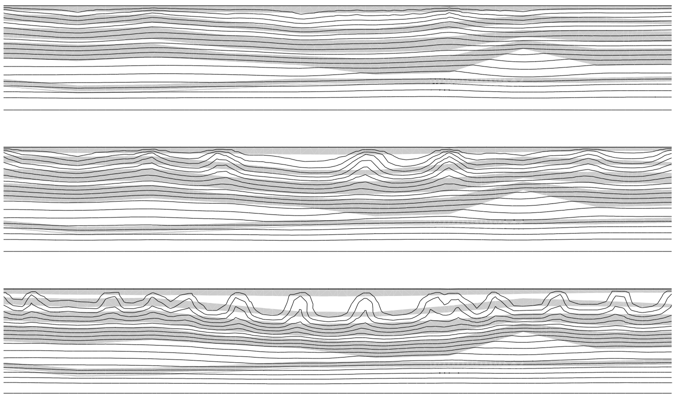

FIGURE 4.11. Stationary, periodic and chaotic solutions after 10 Ma

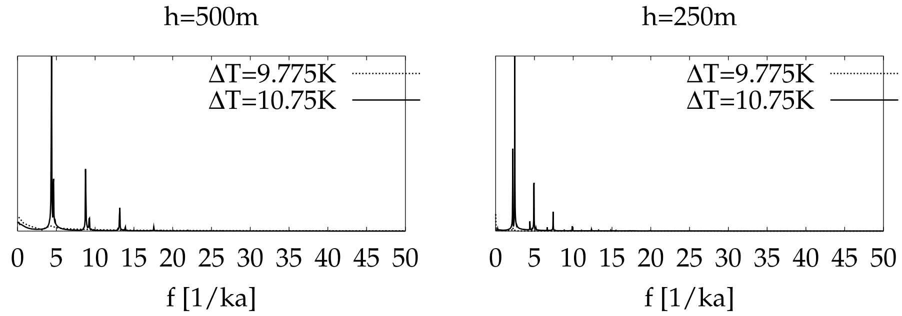

FIGURE 4.12. Onset of quasi-periodic convection in Basin slice 1

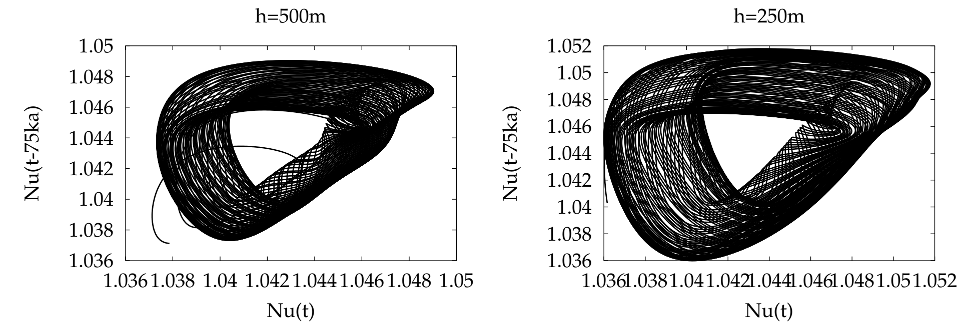

FIGURE 4.13. Phase space reconstruction for onset of quasi-periodic convection in Basin slice 1

4.2. **Basin snapshot 1.**

4.2.1. *Onset of convection.* All calculations in the basin geometries also for very small temperature differences give Nusselt numbers greater than one. This is not

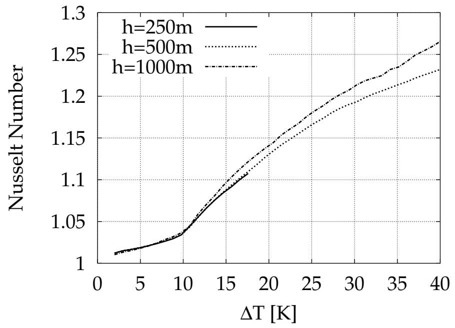

FIGURE 4.14. Time averaged Nusselt number in Basin slice 1

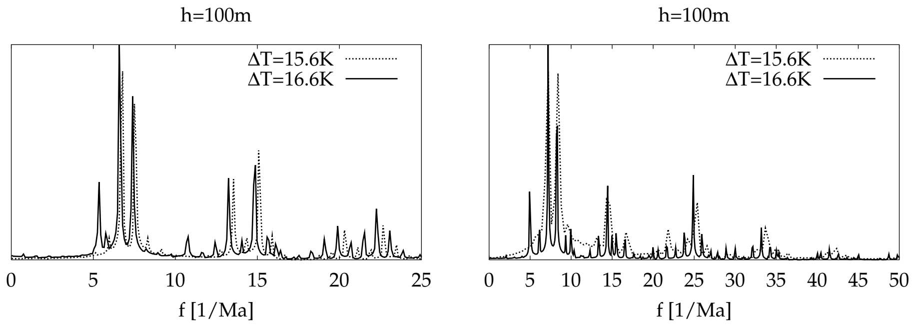

FIGURE 4.15. Lomb periodograms of periodic and chaotic solutions with close temperature gradients (Basin slice 1)

surprising, as the steady state solution corresponding to $Nu = 1$ is bound to the rectangular geometry of the domain. Thus, we always have to expect a – possibly small – amount of convection in our solutions, and a clear bifurcation point where convection starts does not exist.

4.2.2. *Onset of oscillatory convection.* Oscillatory convection in a quasi-periodic manner is detected first for two subsequent meshes for a temperature gradient of 10.75 K/km. This onset of convection, like in the rectangular cavity case, can also be seen from the $\Delta T/Nu$ curves in figure 4.14. There is a kink at the mentioned temperature gradient which possibly indicates a bifurcation.

4.2.3. *Onset of chaos.* An transition to presumed chaos we can see quite well in the frequency domain (fig. 4.15). However in the estimates of the correlation dimension (fig. 4.18), we hardly detect any scaling range. The estimate of the maximal Lyapunov exponent (fig. 4.19) shows a difference in average slopes showing that it becomes larger than 1, thus voting for the chaos hypothesis.

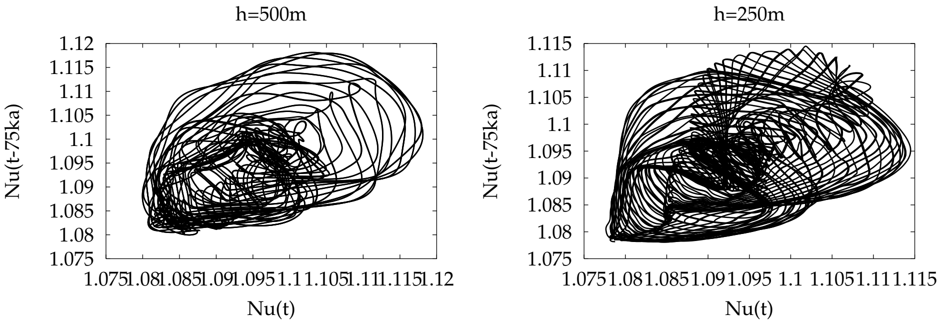

FIGURE 4.16. Phase portrait reconstruction of quasi-periodic solutions (Basin slice 1)

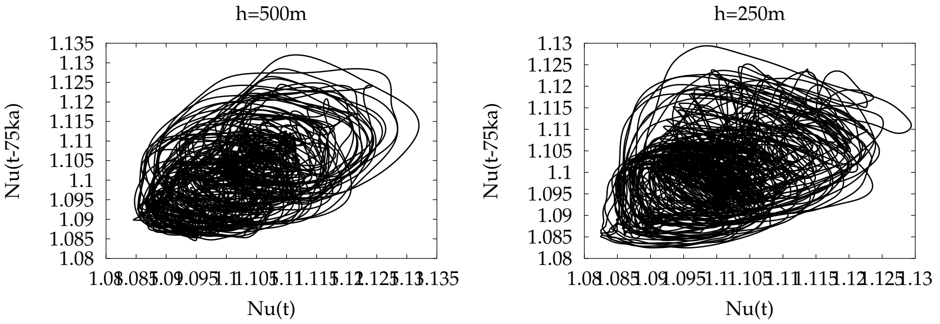

FIGURE 4.17. Phase portrait reconstruction of chaotic solutions (Basin slice 1)

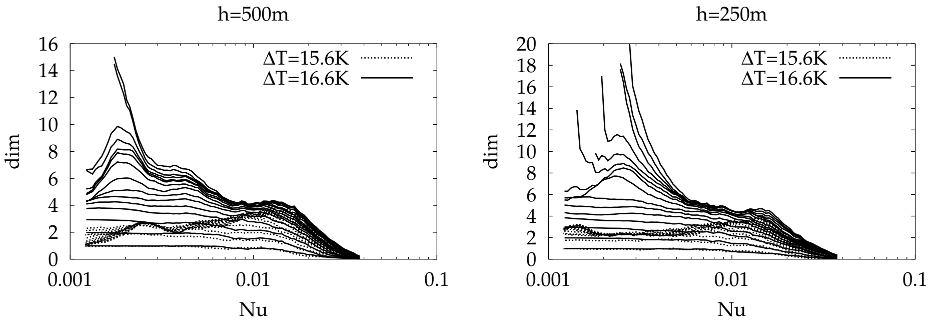

FIGURE 4.18. Estimate of correlation dimension of qusi-periodic and chaotic solutions (Basin slice 1)

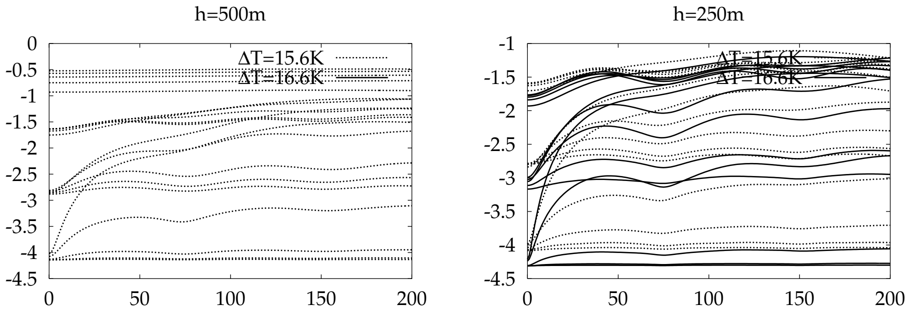

FIGURE 4.19. Estimate of maximal Lyapunov exponent of periodic and chaotic solutions (Basin slice 1)

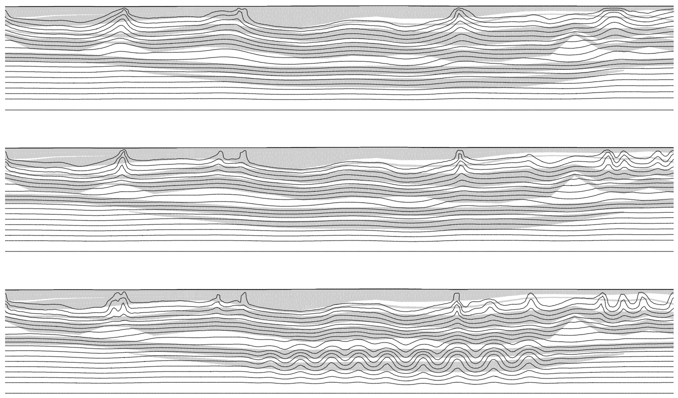

FIGURE 4.20. Stationary, periodic and chaotic solutions after 10 Ma (Basin slice 2)

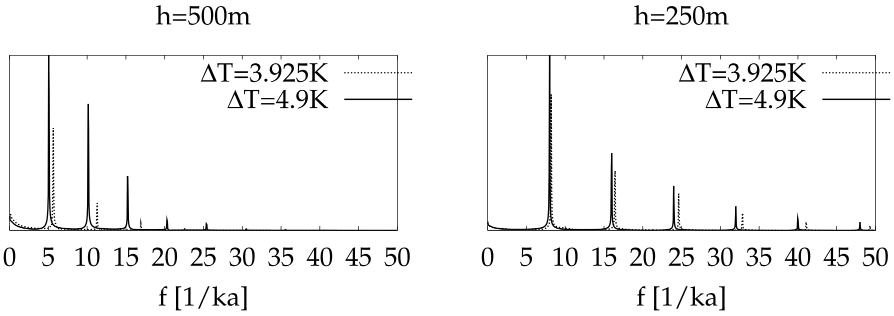

FIGURE 4.21. Onset of periodic convection in Basin slice 2

4.3. **Basin snapshot 2.**

4.3.1. *Onset of convection.* Here, we have to make the same remarks as in 4.2.1.

4.3.2. *Onset of oscillatory convection.* As can be seen in the figures, we see oscillatory convection below the Zechstein layer for much less temperaturee gradients. Obviously, we have to deal with two slightly coupled domains which are due to quasi-periodic/chaotic behaviour. Oscillatory convection in a quasi-periodic manner is detected first for two subsequent meshes for a temperature gradient of 3.925K/km. In the $\Delta T/Nu$ curves in figure 4.23 it can be seen as well.

4.3.3. *Onset of chaos.* Already for a temperature gradient of $6.85K/km$, we see indications of chaotical behaviour. However, the univariate time series analysis as a tool clearly is insufficient to assure this hypothesis.

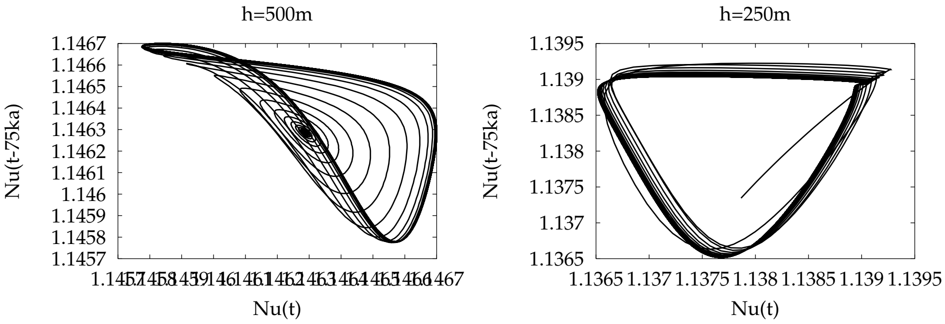

FIGURE 4.22. Phase space reconstruction for onset of periodic convection in Basin slice 2

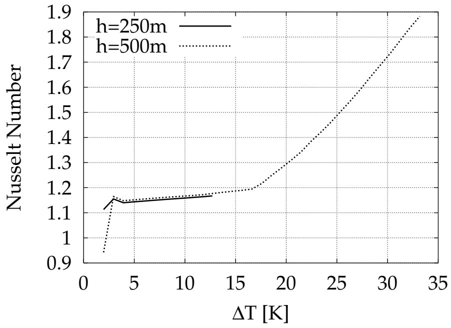

FIGURE 4.23. Time averaged Nusselt number in Basin slice 2

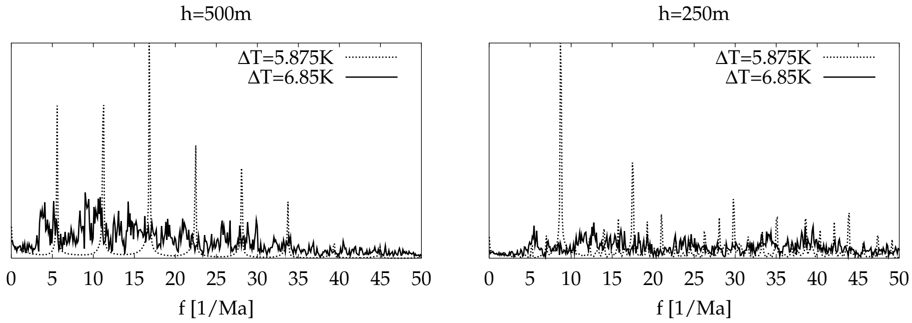

FIGURE 4.24. Lomb periodograms of periodic and chaotic solutions with close parameters (Basin slice 2)

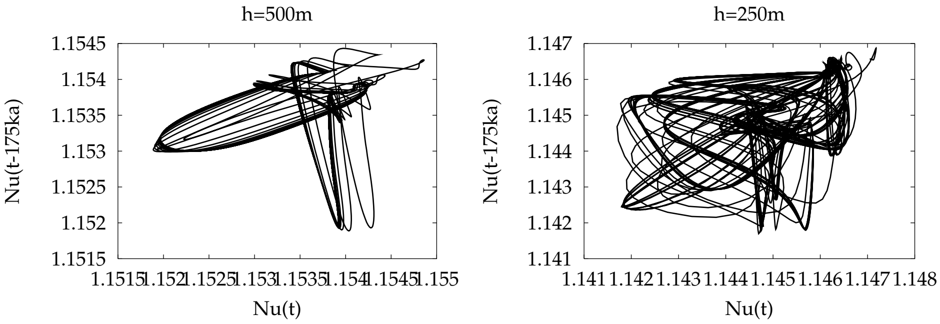

FIGURE 4.25. Phase portrait reconstruction of periodic solutions (Basin slice 2)

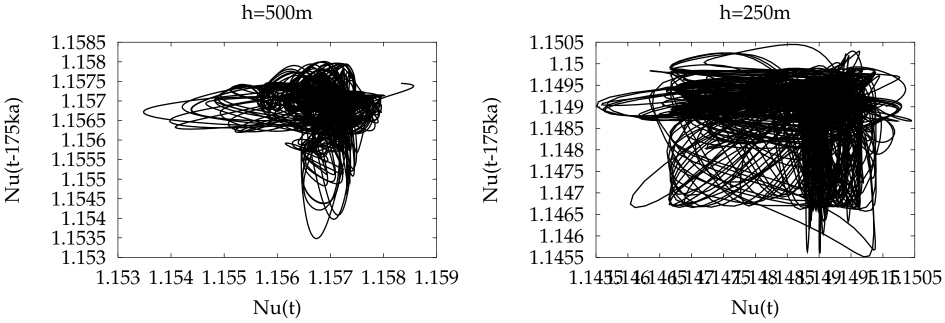

FIGURE 4.26. Phase portrait reconstruction of chaotic solutions (Basin slice 2)

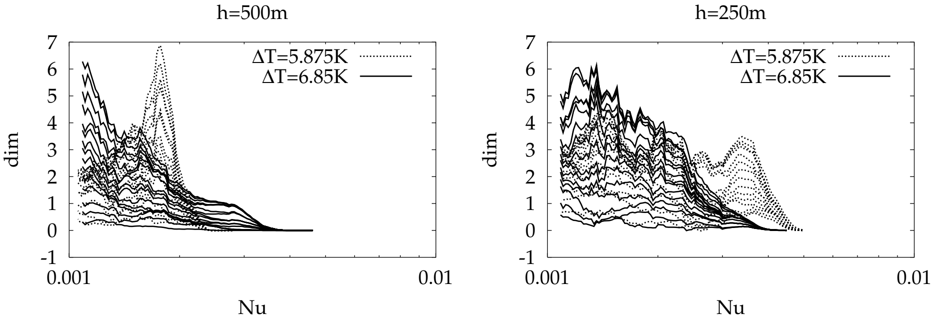

FIGURE 4.27. Estimate of correlation dimension of periodic and chaotic solutions with close parameters

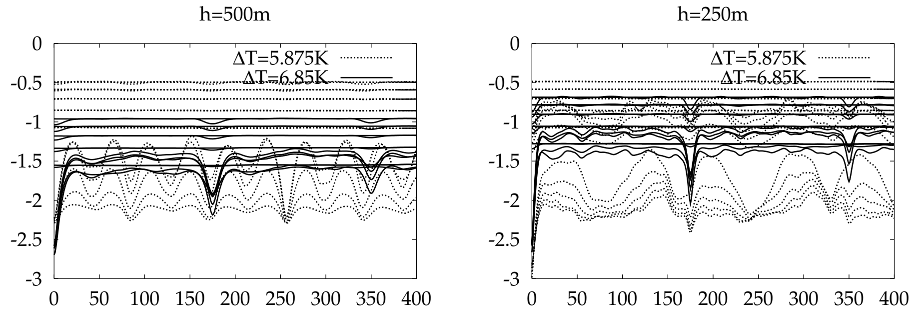

FIGURE 4.28. Estimate of maximal Lyapunov exponent of periodic and chaotic solutions with close parameters (Basin slice 2)

5. Conclusions

In this paper, we presented an approach to the numerical simulation of thermal convection in the deep subsurface which is based on a finite volume upwind method preserving certain characteristics of the physical system. For a rectangular cavity, we have been able to verify the critical Rayleigh number and the consistency of the velocity approximation. Further, in this case we found quasi-periodic oscillations, and chaotic behaviour. Besides from stating the visual evidence of chaos, we could verify this hypothesis by nonlinear time series analysis of the Nusselt number time series obtained from the numerical simulation.

In the case of basin slices, we get quasi-periodic and probably chaotic solutions already at temperature gradients far less than the geological temperature gradient. Visual evidence confirms chaos, however the univariate time series analysis tools readily available are at the borderline of their functioning – according to the warnings of their authors in [KS97, HKS99].

Nevertheless, the possibilty of oscillatory temperature regimes in the deep subsurface calls for further research to be performed, namely

- Addition of salt transport to the model.
- Invariant measure estimates from numerical simulations.
- Three-dimensional simulations calling for improved meshing and solution tools.
- systematic correlation of the simulation output with real occurrences of saline springs

Appendix A. Notations

$\mathbf{x}_i$	i-th node of discretization
ω_i	Voronoi box around $\mathbf{x}_i$
$\omega_i^m = \omega_i \cap \Omega^m$	
$\gamma_{ij} = \overline{\omega_i} \cap \overline{\omega_j}, \quad i \neq j$	interior Voronoi box faces
$\gamma_{ij}^m = \gamma_{ij} \cap \Omega^m$	
$\mathbf{n}_i$	outward unit normal to the Voronoi box boundary
$\mathbf{n}_{ij}, \quad i \neq j$	outward unit normal interior Voronoi box face
$h_{ij} = \mathbf{x}_i - \mathbf{x}_j, \quad i \neq j$	edge lengths

T	Θ	K	Temperature
p	M/LT^2	Pa	Fluid pressure
$\mathbf{v}$	L/T	$m^3/(m^2s)$	volumetric fluid flux density
$\mathbf{q}$	M/T^3	$J/(m^2s)$	heat flux density
ρ_f	M/L^3	kg/m^3	Fluid density
$\tilde{\rho}_f$	M/L^3	kg/m^3	approximate fluid density
ρ_s	M/L^3	kg/m^3	matrix density
c_f	$L^2/(T^2\Theta)$	$J/(kgK)$	specific heat capacity of fluid
c_s	$L^2/(T^2\Theta)$	$J/(kgK)$	specific heat capacity of matrix
k	L^2	m^2	permeability of matrix
λ_f	$ML/(T^3\Theta)$	$J/(Kms)$	heat conduction coefficient of fluid
λ_s	$ML/(T^3\Theta)$	$J/(Kms)$	heat conduction coefficient of matrix
α	L^2/T	m^2/s	thermal diffusivity
μ	M/LT	$Pa \cdot s$	viscosity of fluid
ϕ	L^3/L^3	1	pore space
$\mathbf{g}$	L/T^2	m/s^2	earth acceleration vector
g	L/T^2	m/s^2	earth acceleration
p_{ref}	M/LT^2	Pa	reference pressure of fluid
T_{ref}	M/LT^2	Pa	reference temperature of fluid
ρ_{ref}	M/L^3	kg/m^3	reference density of fluid
β_p	LT^2/M	$1/Pa$	compressibility of fluid
β_T	$1/\Theta$	$1/K$	heat expansion coefficient of fluid
Ra	1	1	Rayleigh Number
H	L	m	characteristic height
v_c	L/T	m	characteristic velocity
T_c	Θ	K	characteristic Temperature difference

APPENDIX B. GEOLOGICAL DATA

Layer	$k_s\ [m^2]$	$\phi\,[1]$	$\rho_s\ \left[\frac{10^3 kg}{m^3}\right]$	$c_s\ \left[\frac{10^3 J}{kg \cdot K}\right]$	$\lambda_s\ \left[\frac{J}{K \cdot m \cdot s}\right]$
Kaenozoikum	10^{-12}	0.23	2.67	1.18	1.5
Oberkreide	10^{-13}	0.1	2.4	1	1.9
Unterkreide	10^{-13}	0.13	2.7	1.18	2
Jura	10^{-13}	0.13	2.7	1.18	2
Keuper	10^{-14}	0.06	2.7	1.18	2.3
Muschelkalk	10^{-18}	0.001	2.4	1	1.85
Buntsandstein	10^{-14}	0.04	2.67	1.18	2
Zechstein	10^{-20}	10^{-6}	2.16	0.84	3.5
ElbeSubgruppe	10^{-14}	0.03	2.67	1	1.84
MirowFormation	10^{-14}	0.03	2.67	1	2.13
ParchimFormation	10^{-14}	0.03	2.67	1	2.4
Vulkanite	10^{-20}	10^{-6}	2.65	0.93	2.5
Praeperm	10^{-20}	10^{-6}	2.7	1	2.65

APPENDIX C. FLUID DATA

We establish our results for a density model found in [Kah82] and a nonlinear viscosity model which we believe to be appropriate for the situation in the deep subsurface.

More precisely, we use

$$
\begin{aligned}
\rho(p,T) =&(-4.261330\cdot 10^{-20}p^2 + 1.473494\cdot 10^{-11}p - 2.483616\cdot 10^{-3})T^2 \\
&+ (+2.732430\cdot 10^{-17}p^2 - 9.720123\cdot 10^{-9}p + 1.155102)T \\
&+ (-4.734071\cdot 10^{-15}p^2 + 2.037606\cdot 10^{-6}p + 8.731945\cdot 10^{2})
\end{aligned} \tag{C.1}
$$

and

$$
\mu(T) = 4.0\cdot 10^7 T^{-4.3195} \tag{C.2}
$$

References

[AS55] D. N. ALLEN AND R. V. SOUTHWELL, *Relaxation methods applied to determine the motion, in two dimensions, of a viscous fluid past a fixed cylinder*, Quart. J. Mech. and Appl. Math., 8 (1955), 129–145.

[BE95] M. W. BERN AND D. EPPSTEIN, *Mesh generation and optimal triangulation*, in Computing in Euclidean Geometry, D.-Z. Du and F. K.-M. Hwang, eds., World Scientific, 1995, 47–123.

[DH79] P. DEUFLHARD AND G. HEINDL, *Affine invariant convergence theorems for Newton's method and extensions to related methods*, SIAM J. Num. Anal, 16 (1979), 1–10.

[EFZ00] M. EFENDIEV, J. FUHRMANN, AND S. ZELIK, *The attractor of the equation of thermpconvective flow in porous media*, tech. rep., WIAS Berlin, 2000. Preprint No. 547, submitted.

[FKL01] J. FUHRMANN, T. KOPRUCKI, AND H. LANGMACH, *pdelib: An open modular tool box for the numerical solution of partial differential equations. Design patterns*, in Proceedings of the 14th GAMM Seminar Kiel on Concepts of Numerical Software, January 23 -25, 1998, Kiel, 2001. Editors: W. Hackbusch and G. Wittum.

[FL01] J. FUHRMANN AND H. LANGMACH, *Stability and existence of solutions of time-implicit finite volume schemes for viscous nonlinear conservation laws*, Applied Numerical Mathematics, 37 (2001) 1-2, 201–230.

[Fro98a] P. FROLKOVIČ, *Consistent velocity approximation for density driven flow and transport*, in Advanced Computational Methods in Engineering, Part 2: Contributed papers, R. V. Keer, B. Verhegge, M. Hogge, and E. Noldus, eds., Maastricht, 1998, Shaker, 603–611.

[Fro98b] ——, *Maximum principle and local mass balance for numerical solutions of transport equation coupled with variable density flow*, Acta Mathematica Universitatis Comenianae, 67 (1998) 1, 137–157.

[Fuh02] J. FUHRMANN, *Multiphysics systems solution by time-implicit Voronoi box finite volumes*, in Finite Volumes in Complex Applications III: Proc. Porquerolles, Paris, 2002, HERMES.

[Hec32] H.-L. HECK, *Das Grundwasser im Zusammenhang mit dem geologischen Bau Schleswig-Holsteins*, Preußische Geol. Landesanstalt, (1932), 106–133.

[HKS99] R. HEGGER, H. KANTZ, AND T. SCHREIBER, *Practical implementation of nonlinear time series methods: The TISEAN package*, CHAOS, 9 (1999), p. 413.

[HS98] M. HANNEMANN AND W. SCHIRRMEISTER, *Paläohydrologische Grundlagen der Entwicklung der Süß-Salzwassergrenze und der Salzwasseraustritte in Brandenburg*, Brandenburgische Geowiss. Beitr., 5 (1998), 61–72.

[HY95] E. HOLZBECHER AND Y. YUSA, *Numerical experiments on free and forced convection in porous media*, Int. J. Heat Mass Transfer, 38 (1995) 11, 2109–2115.

[Il'69] A. M. IL'IN, *A difference scheme for a differential equation with a small parameter multiplying the second derivative*, Mat. zametki, 6 (1969) 2, 237–248.

[Joh80] A. JOHANNSEN, *Hydrogeologie von Schleswig-Holstein*, Geologisches Jahrbuch, Reihe C, Heft 28 (1980).

[KA59] L. V. KANTOROVIČ AND G. P. AKILOV, *Funktional'nyj analiz v normirovannych prostranstvach*, Fiszmatgiz, Moskva, 1959.

[Kah82] O. KAHLE, *Regression der "genauen" Dichtewerte*, in Properties of Water and Steam in SI-Units, E. Schmidt, ed., Springer, Berlin Heidelberg New York, 3rd. printing ed., 1982.

[KS97] H. KANTZ AND T. SCHREIBER, *Nonlinear Time Series Analysis*, Cambridge Univ. Press, 1997.

[Lom76] N. R. LOMB, *Least-squares frequency analysis of unequally spaced data*, Astrophysics and Space Science, 39 (1976), 447–462.

[Mac53] R. H. MACNEAL, *An asymmetrical finite difference network*, Quart. Math. Appl., 11 (1953), 295–310.

[Moo00] G. MOODY, *lomb: Lomb periodogram of real data*. source code, 2000. http://www.physionet.org/physiotools/wfdb/psd/lomb.c.

[NB98] D. A. NIELD AND A. BEJAN, *Convection in Porous Media*, Springer, New York, 1998.

[Rup95] J. RUPPERT, *A Delaunay refinement algorithm for quality 2-dimensional mesh generation.*, Journal of Algorithms, 18 (1995) 3, 548–585.

[SB99] M. SCHECK AND U. BAYER, *Evolution of the Northeast German Basin – inferences from a 3D structural model and subsidence analysis*, Tectonophysics, 313 (1999), 145–169.

[Sch97a] M. SCHECK, *3D structural modeling and evolution of the North-East German Basin*, Terra Nova, 9 (1997), 185–.

[Sch97b] — —, *Dreidimensionale Strukturmodellierung des Norddeutschen Beckens unter Einbeziehung von Krustenmodellen*, tech. rep., GFZ, 1997. STR97/10, 126 pp.

[SG69] D. L. SCHARFETTER AND H. K. GUMMEL, *Large signal analysis of a silicon Read diode*, IEEE Trans. Electronic Dev., 16 (1969), 64–77.

[SGF00] O. SCHENK, K. GÄRTNER, AND W. FICHTNER, *Parallel sparse LU factorization on SMP architectures*, BIT, 40 (2000) 1.

[She96] J. R. SHEWCHUK, *Triangle: Engineering a 2D Quality Mesh Generator and Delaunay Triangulator*, in Applied Computational Geometry: Towards Geometric Engineering, M. C. Lin and D. Manocha, eds., Springer, 1996, 203–222.

[She97] — —, *Delaunay Refinement Mesh Generation*, PhD thesis, School of Computer Science, Carnegie Mellon University, Pittsburgh, 1997. Technical Report CMU-CS-97-137.

[SSH99] S. SCHOOFS, F. SPERA, AND U. HANSEN, *Chaotic thermohaline convection in low-porosity hydrothermal systems*, Earth and Planetary Sciences Letters, 174 (1999), 213–229.

[Tak81] F. TAKENS, *Detecting strange attractors in turbulence*, in Proceedings of the Symposion on Dynamical Systems and Turbulence, Univ. Warwick 1980, D. Rand and L.-S. Young, eds., Berlin, 1981, Springer.

ULF BAYER, GEOFORSCHUNGSZENTRUM POTSDAM, SECTION 4.3, TELEGRAFENBERG C425, D-14473 POTSDAM, bayer@gfz-potsdam.de

VOLKER CLAUSNITZER, WASY GMBH, WALTERSDORFER STRASSE 105, D-12526 BERLIN, vc@wasy.de

JÜRGEN FUHRMANN, WEIERSTRASS INSTITUTE FOR APPLIED ANALYSIS AND STOCHASTICS, MOHRENSTR. 39, D-10117 BERLIN, fuhrmann@wias-berlin.de